UNIVERSITY OF WEST LONDON
The Career University

UWL REPOSITORY

repository.uwl.ac.uk

One-step hydrothermal synthesis of a green NiCo-LDHs-rGO composite for the treatment of lead ion in aqueous solutions

Ata, Makarem, Aldaghi, Alireza, Gheibi, Mohammad, Eftekhari, Mohammad and Behzadian, Kourosh ORCID: https://orcid.org/0000-0002-1459-8408 (2023) One-step hydrothermal synthesis of a green NiCo-LDHs-rGO composite for the treatment of lead ion in aqueous solutions. The Canadian Journal of Chemical Engineering. ISSN 0008-4034

This is a University of West London scholarly output.

Contact open.research@uwl.ac.uk if you have any queries.

Alternative formats: If you require this document in an alternative format, please contact: open.access@uwl.ac.uk

RESEARCH ARTICLE

THE CANADIAN JOURNAL OF
CHEMICAL ENGINEERING

One-step hydrothermal synthesis of a green NiCo-LDHs-rGO composite for the treatment of lead ion in aqueous solutions

Ata Makarem[1] | Alireza Aldaghi[2,3] | Mohammad Gheibi[4] |
Mohammad Eftekhari[5] | Kourosh Behzadian[6,7]

[1]Department of Chemistry, University of Hamburg, Hamburg, Germany

[2]Department of Mechanical Engineering, Ferdowsi University of Mashhad, Mashhad, Iran

[3]Center for Nanotechnology in Renewable Energies, Ferdowsi University of Mashhad, Mashhad, Iran

[4]Institute for Nanomaterials, Advanced Technologies and Innovation, Technical University of Liberec, Liberec, Czech Republic

[5]Department of Chemistry, Faculty of Sciences, University of Neyshabur, Neyshabur, Iran

[6]School of Computing and Engineering, University of West London, London, UK

[7]Department of Civil, Environmental and Geomatic Engineering, University College London, London, UK

Correspondence
Mohammad Eftekhari and Kourosh Behzadian
Email: tekhari@neyshabur.ac.ir and kourosh.behzadian@uwl.ac.uk

Abstract

Herein, we have synthesized a microspherical nickel-cobalt-layered double hydroxides-reduced graphene oxide composite (NiCo-LDHs-rGO) through a one-step hydrothermal method and then used it as an adsorbent for the removal of Pb^{2+} from aqueous solutions. Fourier transform infrared spectrophotometry (FT-IR), field emission scanning electron microscopy (FESEM), mapping elemental analysis, electron dispersive x-ray spectroscopy (EDX), x-ray diffraction analysis (XRD), and the Brunauer–Emmett–Teller (BET) method were used for the characterization of the adsorbent. Factors affecting the adsorption of Pb^{2+} ion such as solution pH, adsorbent dosage, contact time, competing ion, and regeneration were investigated in batch mode by the NiCo-LDHs-rGO. Under optimized conditions based on the Taguchi method (pH = 5.0, adsorbent dosage = 20 mg, and contact time = 30 min), the highest removal percentage was found to be 99.7% for 100 mg L^{-1} of Pb^{2+}. According to the results, NiCo-LDHs-rGO exhibited a high preference for Pb^{2+} over Cu^{2+}, Zn^{2+}, and Cd^{2+}. This adsorbent was regenerated for several cycles (using 0.01 M HCl) with no significant deterioration in performance. Analyses of the adsorption isotherm models revealed that the adsorption of Pb^{2+} follows Freundlich isotherm with a maximum adsorption capacity of 200 mg g^{-1}. Also, the kinetic data confirmed that pseudo second order kinetic equation is the best model for predicting the kinetics. Furthermore, the Simulink modelling illustrated that the adsorption kinetics of Pb^{2+} onto NiCo-LDHs-rGO is done with high accuracy in a continuous stirred-tank reactor. Finally, dual interactions of the effective parameters can be modelled by polynomial equations in MATLAB, and according to the Taguchi model, pH is clearly the most important feature among all effective parameters.

KEYWORDS
lead ion removal, nickel cobalt layered double hydroxides particles-reduced graphene oxide (NiCo-LDHs-rGO), water treatment

1 | INTRODUCTION

Lead (Pb) is a highly toxic element which mainly affects the renal function as well as reproductive and nervous systems.[1] Due to the widespread industrial use of lead in batteries, alloys, pigments, plastic stabilizer, ammunition, glazes, and so forth, its leakage into the environment and surface water samples is considered as one of the most significant environmental challenges.[2,3] According to the reports of the Centers for Disease Control and Prevention, the standard maximum levels of Pb^{2+} for adults and children are 100 and 50 µg/L, respectively.[4] Adsorption is the most popular technique for the treatment of organic and inorganic pollutants, and a wide range of efficient natural and synthetic adsorbents could be used for this purpose.[5–10] The reusability of adsorbents and ease of operation are considered as other advantages of this method.[11–15] In this context, graphene oxide (GO) has been extensively used for the decontamination of water samples.[16–18] Due to the existence of hydroxyl, epoxy, and carboxylic acid groups on its structure, GO is naturally hydrophilic and also can be modified with different functional groups for developing new adsorbents.[19,20] In 2018, Eftekhari et al. modified GO with tannic acid for the elimination of Pb^{2+} in water samples; the resulting nanocomposite showed 250 mg g^{-1} as adsorption capacity in the removal of Pb^{2+}.[21] In 2021, Ghadirimoghaddam et al. used GO-cyanuric acid nanocomposite for the preconcentration/removal of Pb^{2+} with the calculated adsorption capacity of 333 mg g^{-1}.[22] Due to their convenient fabrication, environmental friendliness, and high electrochemical activities, transition metal hydroxides have drawn much attention in the area of supercapacitors[23] and electrocatalysts.[24,25] Despite their high surface area, layered double hydroxides (LDHs) have a high tendency to form aggregation—due to hydrogen-bonding interactions—which consequently reduces the available active sites.[26] To overcome this drawback, high surface-area materials such as graphene[27] and carbon nanotubes[28] can be considered as modifiers.

The purpose of this research is to introduce a new cost-efficient and green adsorbent for the treatment of Pb^{2+}. Hence, we have synthesized a microspherical nickel cobalt layered double hydroxides particles-reduced graphene oxide (NiCo-LDHs-rGO) composite using a one-step hydrothermal method, and then examined it in the removal of Pb^{2+} from aqueous media. The synthesized composite was characterized by field emission scanning electron microscopy (FESEM), x-ray diffraction analysis (XRD), electron dispersive x-ray spectroscopy (EDX), mapping elemental analysis, and Fourier transform infrared (FT-IR) spectrophotometry. Parameters affecting the removal percentage (RP) of Pb^{2+} were optimized by the Taguchi design method, while the kinetics and mechanism of adsorption were investigated by different kinetic and isotherm models.

2 | EXPERIMENTAL

2.1 | Instruments

The following instruments and techniques were used in this study: (1) A BRNO-Mira3 LMU instrument manufactured by TESCAN in Czech Republic for FESEM, EDX, and mapping elemental analysis. FESEM was used to visualize the microstructure and surface morphology of the composite. EDX provided information concerning the elemental composition of the composite, while mapping elemental analysis enabled the spatial distribution of elements within the composite; (2) FT-IR spectra were recorded using an AVATAR 370 (USA); (3) The XRD analysis was carried out using a D8-Advance Bruker Cu Kα1 instrument (USA); (4) The specific surface area of the composite was determined using a Belsorp-Mini instrument (Japan); (5) In order to quantify the Pb^{2+} concentration (after adsorption), an electrothermal atomic absorption spectrometer equipped with a Pb hollow cathode lamp (283.3 nm) was used (Perkin Elmer Analyst 700, USA). Argon (99.99%) was used as the inert atmosphere, with a flow rate of 300 mL min^{-1} during drying, ashing, and cleaning stages, and zero during the atomization step; (6) For the adjustment of pH during the adsorption experiments, a Metrohm 827 pH-meter (Switzerland) was used; (7) The separation of the adsorbent from the solution was carried out using an Andreas Hettich D72 centrifuge instrument (Germany).

2.2 | Reagents

Lead nitrate (Merck, Germany) was used to make a 1000 mg L^{-1} Pb^{2+} solution. Graphite (99.9%), $Co(NO_3)_2 \cdot 6H_2O$ (99.5%), $Ni(NO_3)_2 \cdot 6H_2O$ (99.5%), H_2SO_4 (98.0%), $KMnO_4$ (99.0%), H_2O_2 (30.0%), thiourea, and HNO_3 (65.0%) were supplied by Merck (Germany).

2.3 | Synthesis of GO and NiCo-LDHs-rGO

First, GO was synthesized according to the Hummers method as presented in Figure 1.[21] The NiCo-LDHs-rGO composite was then synthesized according to the following protocol: GO (0.35 g) was ultrasonicated in 50 mL of deionized water for 45 min. Then, $Co(NO_3)_2 \cdot 6H_2O$ (0.40 g),

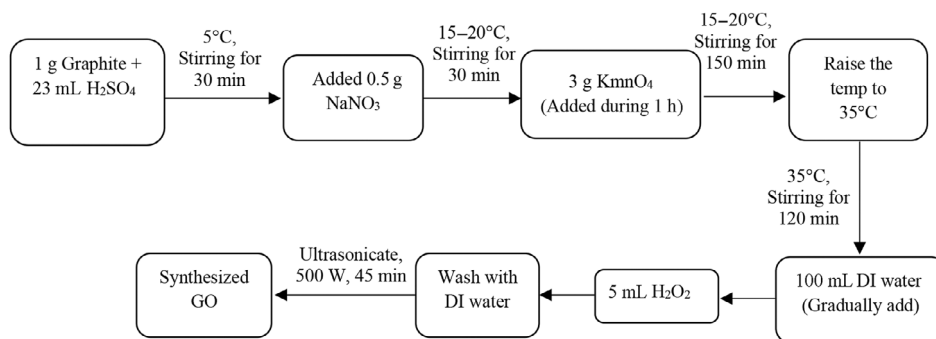**FIGURE 1** Synthetic route of graphene oxide (GO). DI, deionized water.

Ni(NO₃)₂ · 6H₂O (0.30 g), and thiourea (0.10) were added. The resulting mixture was ultrasonicated for another 30 min and then autoclaved at 160°C for 4 h. The obtained composite was washed with deionized water (three times) and dried at 90°C (6 h).

2.4 | Removal procedure

To 10 mL of a 100 mg L^{-1} Pb^{2+} solution (pH 5.0), 20 mg of the NiCo-LDHs-rGO composite was added, and the mixture was stirred at 500 rpm for 60 min. The concentration of remaining Pb^{2+} was quantified by atomic absorption spectroscopy. Equations (1) and (2) were used for calculating the RP and the adsorption capacity (q_e), respectively.

$$RP = \frac{(C_0 - C_e)}{C_0} \times 100 \qquad (1)$$

$$q_e = \frac{(C_0 - C_e) \times V}{m} \qquad (2)$$

where C_e and C_0 are equilibrium and initial concentration of Pb^{2+} (mg L^{-1}), V is sample volume (L), and m is adsorbent dosage (g).

3 | RESULTS AND DISCUSSION

3.1 | Characterization of adsorbent

The formation of NiCo-LDHs-rGO can be justified by a mechanism proposed in the literature.[29] According to this, first, thiourea is oxidized by GO resulting in NH₄OH (aqueous) and rGO. Then, the OH$^-$ ion reacts with Ni^{2+} and Co^{2+}, forming a network of Ni(OH)₂ and Co(OH)₂ complex species on the surface of reduced GO.[29,30] It is worth noting that organosulphur reagents such as thiourea, thiols, and sulfones are a useful tool for the functionalization of organic materials.[30] Our group has

been investigating the structural features of metal-complex systems for a couple of years.[31]

The synthesized NiCo-LDHs-rGO material was characterized by FESEM, EDX, mapping elemental analysis, FT-IR spectrophotometry, Brunauer–Emmett–Teller (BET), and XRD. According to the FESEM images of NiCo-LDHs-rGO (presented in Figure 2), spherical NiCo-LDHs microparticles have uniformly grown on the rGO nanosheets. The EDX analysis (Figure 3) confirms that Co, Ni, C, and O are the main elements in the structure of this composite.

Also, the mapping elemental analysis of NiCo-LDHs-rGO, presented in Figure 4A–D, displays a distribution of C (4A), O (4B), Ni (4C), and Co (4D) elements. According to the results, the microspheres NiCo-LDHs contain Ni, Co, and O atoms; nevertheless, C atoms have been concentrated on the rGO nanosheet. Moreover, the low distribution of O atoms on the rGO nanosheet clearly confirms the effective conversion of GO to rGO.

In the FT-IR spectrum of GO (Figure 5), the bands at 1050, 1220, 1730, and 3400 cm^{-1} are attributed to the stretching vibrations of C—O, epoxy, carbonyl (C═O), and O—H groups, respectively.[32] However, for NiCo-LDHs-rGO, the peaks at 1388 and 832 cm^{-1} are related to intercalated NO₃$^-$ (Figure 5).[29,33] The absorbance at 1480 cm^{-1} belongs to the C—H stretching vibration, while the broad band at about 650 cm^{-1} could be related to Ni—O and Co—O vibrations.[33] Moreover, the absorption band at 3400 cm^{-1} is attributed to the stretching vibration of the OH group of NiCo-LDHs, rGO, and/or adsorbed water molecules.

In order to calculate the surface area of NiCo-LDHs-rGO, BET analysis was conducted (Figure S1 in Electronic Supplementary Material); based on the results, the composite possesses slit-shaped pores (H3) since it shows type IV of the isotherm with the hysteresis at $P/P0 = 0.34$–0.97. Also, the calculated average pore diameter and surface area were 18.8 nm and 50.2 m^2 g^{-1}, respectively; this confirms that the composite has a mesoporous structure (2–50 nm pore diameter). Finally, XRD analysis of NiCo-LDHs-rGO (Figure S2) showed that the diffraction peaks at
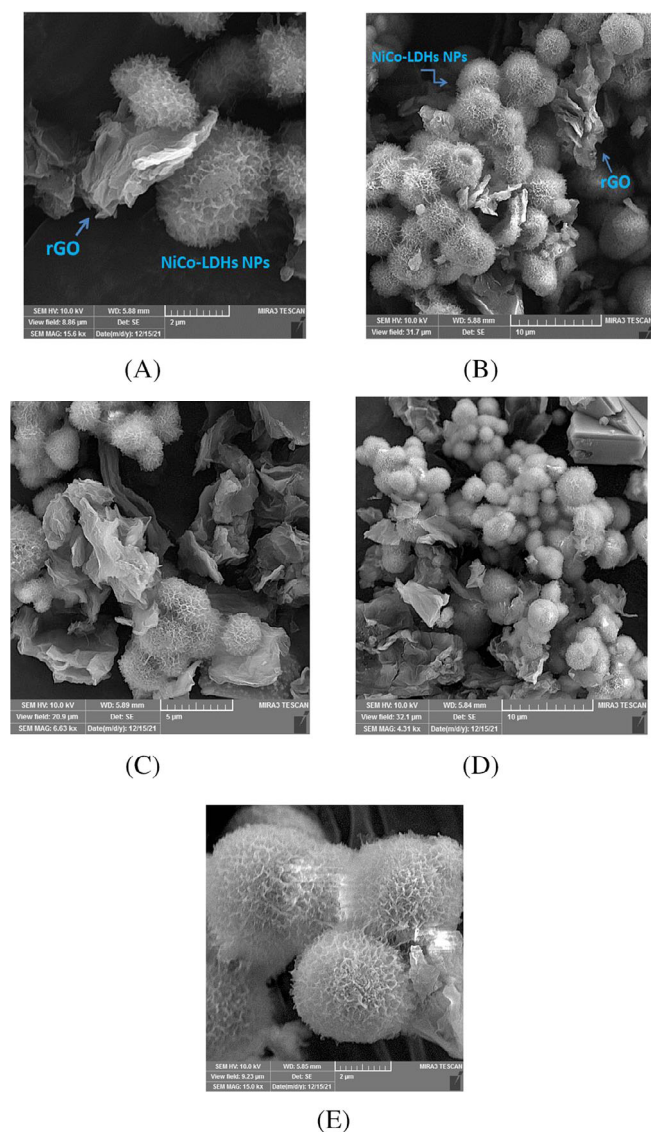
(A)

(B)

(C)

(D)

(E)

FIGURE 2 Field emission scanning electron microscopy (FESEM) images of the synthesized nickel cobalt layered double hydroxides particles-reduced graphene oxide (NiCo-LDHs-rGO).

$2\theta = 11.2°$, $34.0°$, $38.5°$, and $60.5°$ can be indexed to (003), (009), (015), and (110) crystal planes, respectively (JCPDS No. 38-0715).[34] Moreover, the intense diffraction main peak of rGO—appearing at approximately $2\theta = 24.0°$—confirms that GO has been effectively converted to rGO.[35]

3.2 | Optimisation of critical parameters

Outputs of the normal diagram evaluation for all experimental practices in the removal process—including pH, amounts of adsorbent (M), and contact time (CT)—are illustrated in Figure 6. It is understood that all the mentioned features follow a normal statistical distribution. It is worth noting that the optimization process was accomplished by the Taguchi design method.
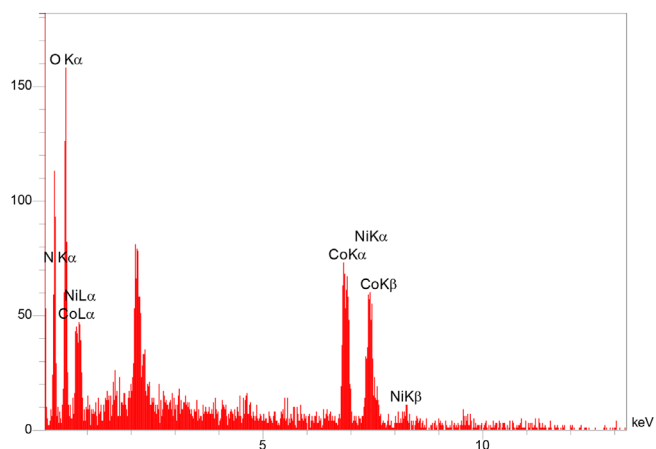

FIGURE 3 Electron dispersive x-ray spectroscopy (EDX) analysis of nickel cobalt layered double hydroxides particles-reduced graphene oxide (NiCo-LDHs-rGO).
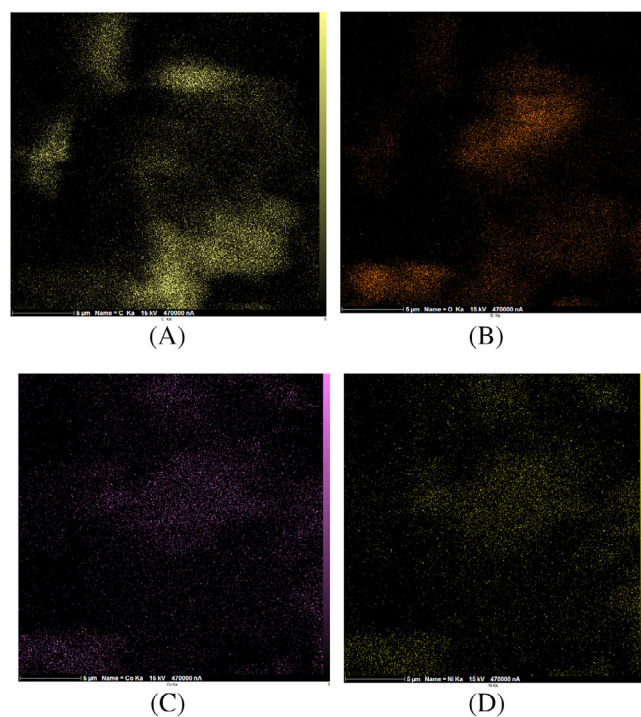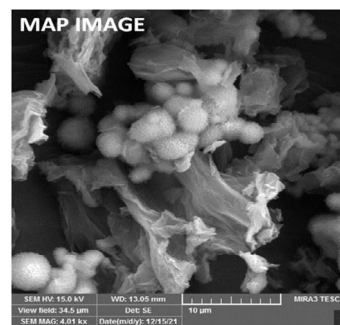

(A)

(B)

(C)

(D)

FIGURE 4 Mapping elemental analysis of nickel cobalt layered double hydroxides particles-reduced graphene oxide (NiCo-LDHs-rGO); distribution of C, O, Co, and Ni atoms (A–D).
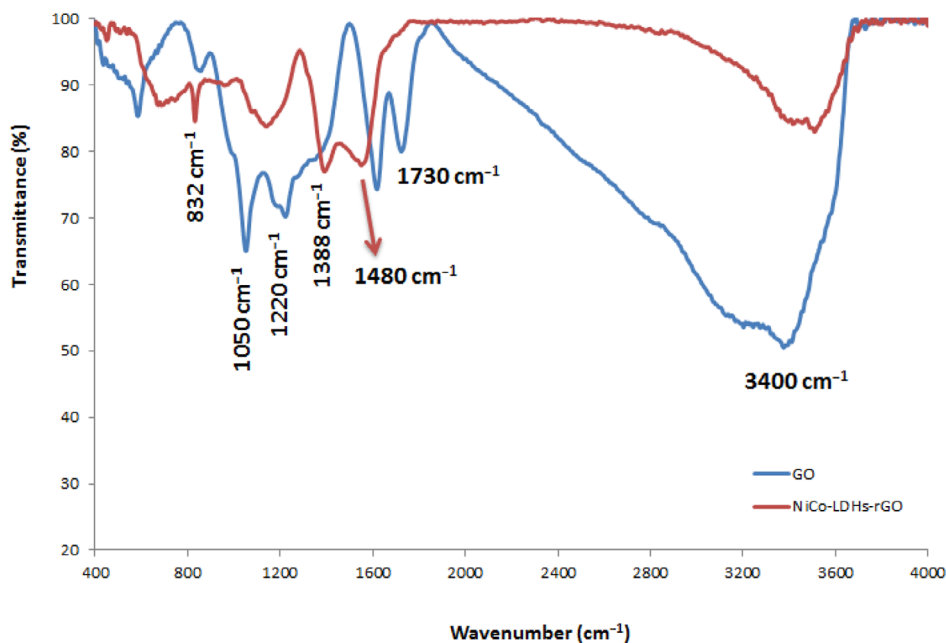
FIGURE 5 Fourier transform infrared (FTIR) spectra of graphene oxide (GO) and synthesized nickel cobalt layered double hydroxides particles-reduced graphene oxide (NiCo-LDHs-rGO).
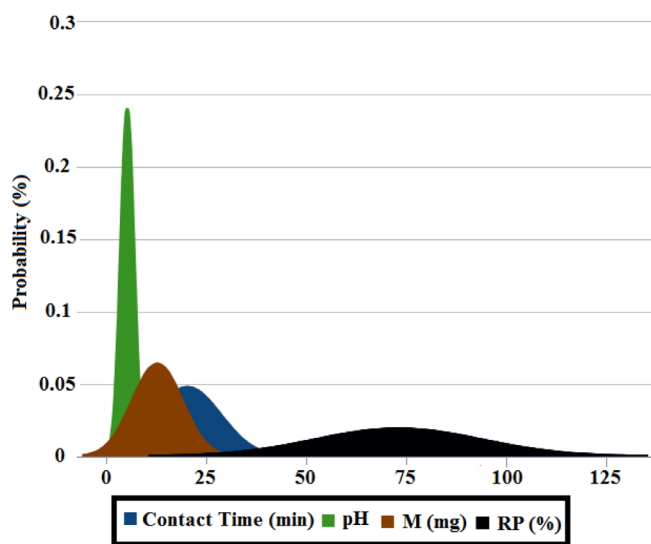

FIGURE 6 Normal distribution examination for input and output design of experiment process. RP, removal percentage.

TABLE 1 Specification of the effective parameters in Taguchi model.

Parameters/levels	I	II	III
pH (A)	3.0	5.0	7.0
M (mg, B)	5.0	12.5	20.0
CT (min, C)	10.0	20.0	30.0
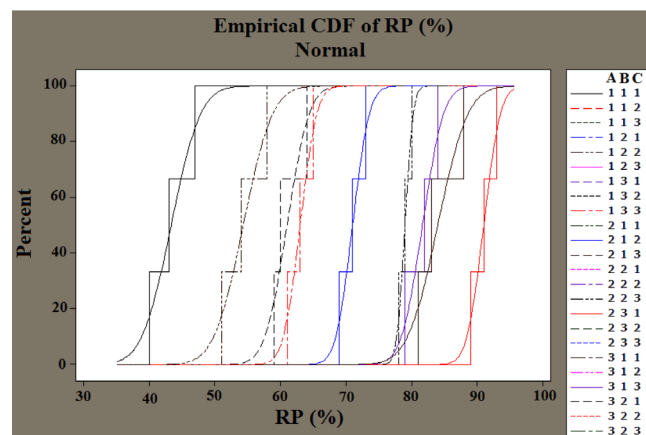
FIGURE 7 The outputs of cumulative distribution function (CDF) computations in the present research. RP, removal percentage.

Limitations and effective parameters concerning the RP (%) are detailed in Table 1.

The outputs of cumulative distribution function (CDF) are presented in Figure 7, which are based on the statistical analysis of RP (%) in different experiments (each curve represents a different run). The vertical axis shows the probability of RP in a specific examination. According to the results, it is obvious that by setting the pH value at the second parameter (level II, pH = 5.0, Table 1), the performance of adsorption process increases dramatically. To study the adsorption mechanism of Pb^{2+}, the pH_{PZC} of NiCo-LDHs-rGO composite was determined as 3.8 (Figure S3). Therefore, due to the deprotonation effect, the surface of NiCo-LDHs-rGO was negatively charged at pH > 3.6. The adsorption mechanisms of Pb^{2+} nto the adsorbent could be explained by the following mechanisms: (1) Electrostatic interaction between the remaining carboxylic acid groups of rGO and Pb^{2+} (Figure 8, mechanism 1); (2) Ion-dipolar interaction between the hydroxyl groups of NiCo-LDHs and rGO

FIGURE 8 The mechanism of
Pb^{2+} adsorption onto the nickel
cobalt layered double hydroxides
particles-reduced graphene oxide
(rGO-NiCo LDHs).
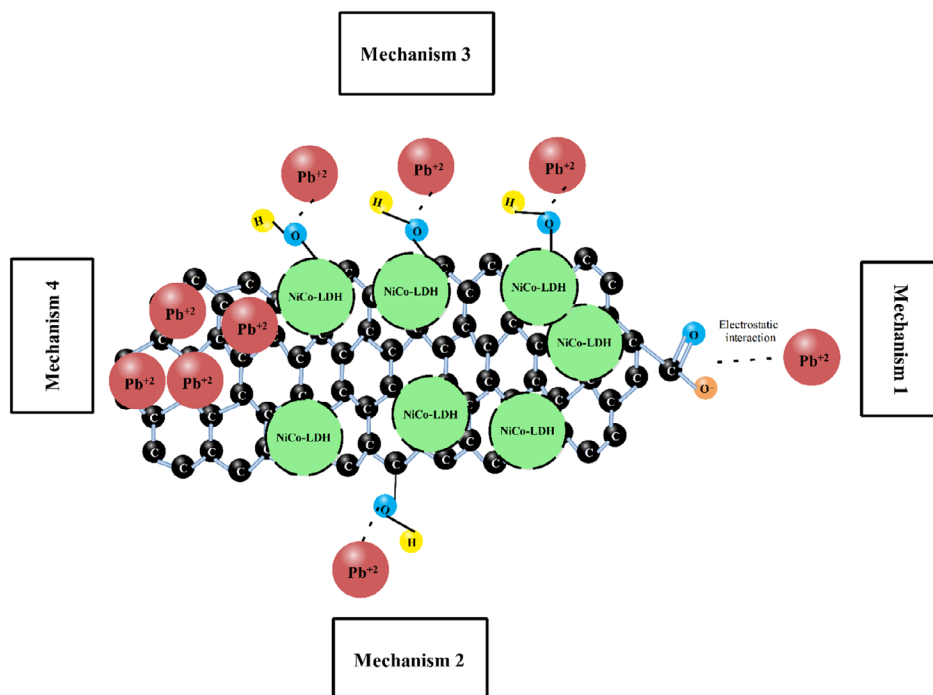
and the Pb^{2+} ion (Figure 8, mechanisms 2 and 3); and
(3) π–cation interaction between rGO and Pb^{2+}
(Figure 8, mechanism 4). All in all, it is expected that in
acidic pH (level I, pH = 3.0), the RP of Pb^{2+} decreases
due to the large amount of H$^+$ ions competing with
Pb^{2+} ions, which occupy the adsorption sites of NiCo-
LDHs-rGO and hinder the dissociation of carboxylic acid
for electrostatically interacting with Pb^{2+} ions.[36–43]
According to Figure 7, it is observed that when all effec-
tive factors are at the first level (black line in Figure 7),
the RP almost reaches 50% (in the best situation). This is
despite the fact that in the optimal state it can reach over
95% (red line in Figure 7). Figure S4 represents the
EDX analysis of NiCo-LDHs-rGO after adsorption.
The appearance of a Pb^{2+} peak at 10.5 keV clearly shows
that Pb^{2+} ions have been adsorbed effectively.

Signal-to-noise (S/N) ratio evaluation (Taguchi
method, Figure 9) has been performed by the Minitab 16
software. By focusing on the scheme, it is found that for
the first parameter (pH), the second level (pH = 5.0)
has the most efficiency with the highest S/N ratio
value. Additionally, the optimum conditions of M and
CT are related to the third values (M = 20.0 mg and
CT = 30.0 min). Likewise, the dual sensitive analysis of the
effective parameters is illustrated in Figure 10. The S/N
value indicates the strength of signal against noise in
electrical systems.[44] This is despite the fact that, in the
Taguchi method, the same concept is used to determine
the optimality of each parameter at different levels.[45]
Therefore, a higher value of S/N is accompanied by higher
efficiency of the system.[46]
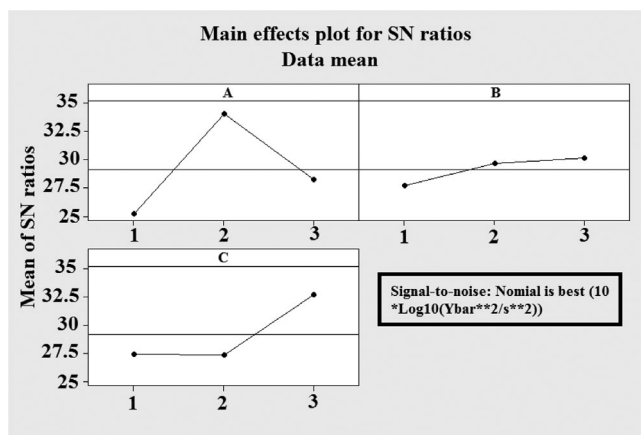
FIGURE 9 Outputs of Taguchi computation in the
present research (A: pH, B: M, C: contact time [CT]). SN,
signal-to-noise.

Figure 10 provides a binary sensitivity analysis of the
key parameters in relation to the removal efficiency. In
Figure 10A, it is evident that the slope fluctuations for
the pH are more pronounced compared to the parameter M.
This observation suggests that the obtained response (RP)
is more influenced by the pH parameter rather than M.
Additionally, the analysis of Figure 10B,C leads to the
conclusion that pH is the most influential factor on
RP. These findings highlight the significance of pH in the
determination of RP and overall effectiveness of the
decontamination process. Comparing Figure 10A–C
reveals valuable aspects of the decontamination process
using the newly synthesized composite. It is evident that

FIGURE 10 The outputs of dual sensitive analysis: (A) pH–M, (B) pH–contact time (CT), and (C) M–CT. RP, removal percentage.

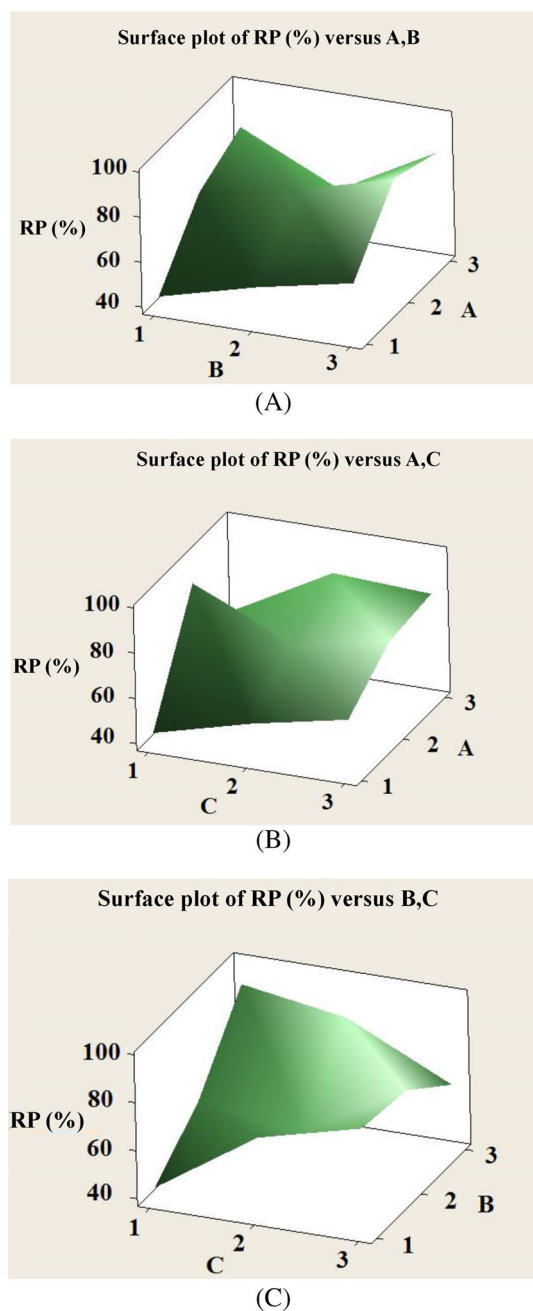A has a greater influence than B, A has a greater influence than C, and C has a greater influence than B. Consequently, the order of importance for these parameters can be established as follows: A > C > B. Furthermore, the intensity of slope variation, Figure 9, supports the same conclusion. The S/N values obtained from the factor A are consistently higher than those of factors C and B. This reaffirms the importance of factor A (pH) in driving the response and underscores its significant role for the optimisation of the

decontamination process. By providing a more comprehensive analysis and highlighting the consistent trends, observed across multiple figures, the extended passage offers greater clarity regarding the importance of the pH parameter related to the response variable (RP), emphasizing its critical role in the decontamination process.

Based on pH, M, and CT, a polynomial regression model has been utilized for the RP. The correlation coefficients of quadratic models for the interpolation of M–pH (Equation (3) and Figure 11A), CT–pH (Equation (4) and Figure 11B), and M–CT (Equation (5) and Figure 11C) are equal to 0.62, 0.67, and 0.47, respectively. However, due to the low values of the coefficients, it is understood that the proposed methods could not predict the RP, and thus, machine learning computations are suggested.

$$f(x,y) = p00 + p10*x + p01*y + p20*x^2 + p11*x*y \\ + p02*y^2 \tag{3}$$

Coefficients (with 95% confidence bounds): $p00 = -74$ $(-157.2, 9.234)$; $p10 = 52.66$ $(21.46, 83.86)$; $p01 = 0.1962$ $(-5.947, 6.339)$; $p20 = -4.246$ $(-7.264, -1.229)$; $p11 = -0.2695$ $(-0.8385, 0.2995)$; $p02 = 0.09634$ $(-0.1183, 0.3109)$.

$$f(x,y) = p00 + p10*x + p01*y + p20*x^2 + p11*x*y \\ + p02*y^2 \tag{4}$$

Coefficients (with 95% confidence bounds): $p00 = -85.21$ $(-170.9, 0.4487)$; $p10 = 47.66$ $(18.37, 76.960)$; $p01 = 2.853$ $(-2.09, 7.7970)$; $p20 = -3.499$ $(-6.301, -0.6977)$; $p11 = -0.2947$ $(-0.6909, 0.1015)$; $p02 = -0.01909$ $(-0.1312, 0.0929)$.

$$f(x,y) = p00 + p10*x + p01*y + p20*x^2 + p11*x*y \\ + p02*y^2 \tag{5}$$

Coefficients (with 95% confidence bounds): $p00 = 1.23$ $(-68.99, 71.45)$; $p10 = 3.595$ $(-3.471, 10.66)$; $p01 = 3.94$ $(-2.144, 10.02)$; $p20 = 0.06327$ $(-0.1937, 0.32)$; $p11 = -0.1966$ $(-0.3329, -0.06)$; $p02 = -0.02491$ $(-0.1694, 0.12)$.

Lazy learning is a type of machine learning computation, and the main purpose of this tool is related to some attribute data specifications. Also, due to the limited characterization of the adsorption process in comparison to other data mining examples, the lazy models were applied in the present research. Following the investigation, lazy.IBk, lazy.KStar, and lazy.LWL have been checked since the efficiency of the mathematical regression modelling was low. The data distribution through
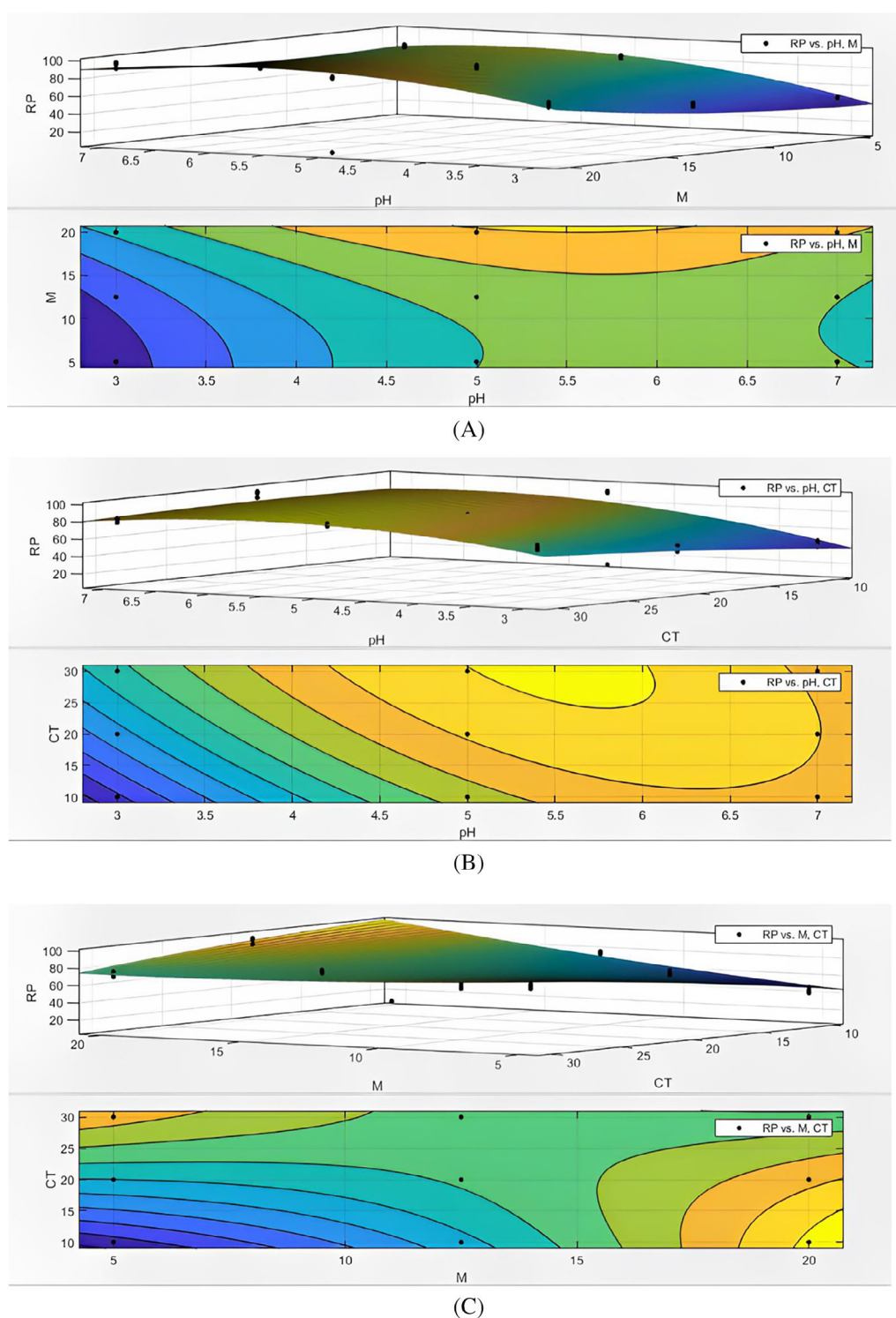
FIGURE 11 Outputs of dual mathematical modelling based on removal percentage (RP) fluctuations. (A) pH–M, (B) pH–contact time (CT), and (C) M–CT.

data mining computations is presented in Figure 12. To implement machine learning systems, different structuring should be applied to the input data. As observed in Figure 12, the learning data is displayed as a matrix plot. This is while the data specified in the

mentioned figure have been obtained from experiments and thus are the output of practical processes. According to Table 2, it can be assumed that all the computations have appropriate performance with a correlation coefficient more than 0.9500 for the prediction of RP;

the approach can fill the lack of precision in simple mathematical modelling.

3.3 | Adsorption isotherm

3.3.1 | Langmuir and Freundlich

Equation (6) (Table S1) shows the Langmuir isotherm which is related to monolayer adsorption. The calculated q_{max} and K_{ads} are 200 mg g^{-1} and 13.44 L mg^{-1}, respectively (Table 3).[29] Moreover, Equation (7) shows the multilayer adsorption of the analyte (Table S1) based on the Freundlich isotherm. The calculated Freundlich parameters (Table 3) show that the adsorption of Pb^{2+} onto the NiCo-LDHs-rGO composite is a favourable process ($n > 1$).[29] Also, since the R^2 values of

Langmuir (0.9930) and Freundlich (0.9860) isotherms were very close to each other, three-parameter isotherm models were used to determine the accurate adsorption isotherm model.[29]

3.3.2 | Three-parameter isotherm

In order to determine the adsorption mechanism exactly, three-parameter isotherms including those of Sips,[47] Koble and Corrigan,[48] Toth,[49] Khan et al.,[50] and the Radke–Prausnitz model[51] were employed. The outcome and conditions of each isotherm are illustrated in Table 4. According to the results, it is understood that the Freundlich model—which follows the heterogeneous surface adsorption mechanism—dominated the monolayer system.

3.3.3 | Dubinin–Radushkevich (DR) model

Equation (8) (Table S1) shows the DR isotherm formula (Equations (9) and (10) have been used for the calculation of DR factors). According to the physical adsorption mechanism ($E < 8.00$ kJ/mol) and also the obtained E value presented in Table 3 ($E = 1.30$ kJ/mol), it is concluded that a physio-sorption process has occurred for Pb^{2+} adsorption.[29]

3.3.4 | Temkin model

Equation (11) (Table S1) shows the Temkin model. According to the b value presented in Table 3 ($b = 93.51$ J/mol), the Pb^{2+} adsorption is a physical process. The diagrams of Langmuir, Freundlich, DR, and Temkin isotherms are presented in Figure S5.
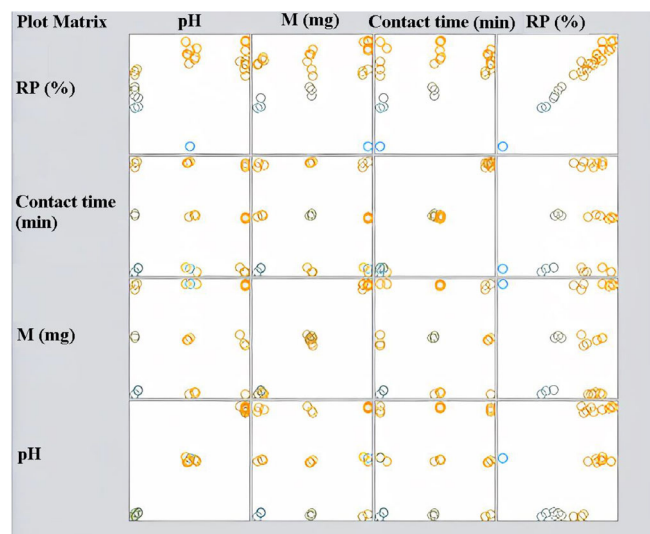
FIGURE 12 Data distribution in this study. RP, removal percentage.

TABLE 2 Results of lazy.IBk, lazy.KStar, and lazy.LWL modelling.

Parameters	Lazy.IBk	Lazy.KStar	Lazy.LWL
Correlation coefficient	0.9927	0.9922	0.965
Mean absolute error	3.6667	4.7041	7.2196
Root mean squared error	4.2622	5.7238	8.4789
Relative absolute error	23.4043%	30.0262%	46.0824%
Root relative squared error	21.7036%	29.1459%	43.1752%
Description	Instances: 27 Attributes: 4 Test mode: split 66.0% train, remainder test IB1 instance-based classifier	Relation: ML Instances: 27 Attributes: 4 Test mode: split 66.0% train, remainder test KStar Beta Verion (0.1b). KStar options: −B 20 −M a	Relation: ML Instances: 27 Attributes: 4 Test mode: split 66.0% train, remainder test Locally weighted learning Using classifier: weka. classifiers.

TABLE 3 Results of interpretation of isotherm models.

Isotherm	Coefficients			
Langmuir Isotherm	q_{max} (mg g^{-1})	k_{ads} (L g^{-1})	R^2	
	200	13.44	0.9930	
Freundlich Isotherm	N	k_F	R^2	
	3.99	47.55	0.9860	
Temkin Isotherm	b (J/mol)	A (L mg^{-1})	R^2	
	93.51	4.21	0.9394	
D–R Isotherm	q_{max} (mg g^{-1})	k_d (mol^{2}J^{-2})	R^2	E (kJ(mol)$^{-1}$)
	134	0.34	0.7061	1.30

Abbreviation: D–R, Dubinin–Radushkevich.

TABLE 4 The results of three-parameter isotherm.

Three-parameter isotherm	Formulation	Description	Correlation coefficient	Selected mechanism
Sips	$q_e = \frac{k_s C_e{}^{\beta_s}}{1 + a_s C_e{}^{\beta_s}}$	If B_t converge to 1, Langmuir is the main mechanism; else, Freundlich is the appropriate mechanism.	0.98	Heterogeneous surface mechanism (Freundlich)
Koble–Corrigan	$q_e = \frac{A C_e{}^n}{1 + B C_e{}^n}$	If n converge to 1, Langmuir is the main mechanism; else, Freundlich is the appropriate mechanism.	0.98	Heterogeneous surface mechanism (Freundlich)
Toth	$q_e = \frac{k_T C_e}{(a_T + C_e)^{1/t}}$	If $1/t$ converge to 1, Langmuir is the main mechanism; else, Freundlich is the appropriate mechanism.	0.98	Heterogeneous surface mechanism (Freundlich)
Khan	$q_e = \frac{q_s b_k C_e}{(1 + b_k C_e)^{u_k}}$	If u_t converge to 1, Langmuir is the main mechanism; else, Freundlich is the appropriate mechanism.	0.98	Heterogeneous surface mechanism (Freundlich)
Radke–Prausnitz	$q_e = \frac{a_{RP} r_R C^{\beta_R}{}_e}{a_{RP} + r_R C^{\beta_R - 1}{}_e}$	If $B_R - 1$ converge to 1, Langmuir is the main mechanism; else, Freundlich is the appropriate mechanism.	0.98	Heterogeneous surface mechanism (Freundlich)

3.4 | Adsorption kinetic

3.4.1 | Pseudo first order kinetic model (PFO model)

The formula of the PFO model is provided in Table S2 (Equation (12)).[29] As described in Table 5, the R^2 values for Pb^{2+} are in the range of 0.6678–0.7459. Moreover, the calculated q_e is different than the experimental q_e; accordingly, PFO is not applicable for analyzing the kinetic results.

3.4.2 | Pseudo second order model (PSO model)

Equation (13) (Table S2) represents the simplified form of the PSO model.[29] Table 5 displays the calculated values

of k_2 and R^2, so that R^2 was obtained as ≥0.9800 for different Pb^{2+} concentrations. Also, q_e (cal) is so close to q_e (exp), showing that PSO is the applicable model for analyzing the kinetic data.

3.4.3 | Intraparticle diffusion (ID) model

Equation (14) (Table S2) displays the formula of the ID model, while Figure 13 presents the obtained ID plots for different concentrations of Pb^{2+}. As observed, the plots have two zones: (1) A faster zone contributing to the diffusion of analytes from the bulk solution to the adsorbent surface; and (2) A slower zone which is related to the ID.[29] The obtained R^2 values of the two zones and as well as calculated k_{int} are shown in Table 5.

Concentration (mg L^{-1})			50	100	200	400
q_e(exp)		mg g^{-1}	51	99	177	236
PFO model	k_1	1/min	0.030	0.020	0.018	0.018
	q_e	mg g^{-1}	10	35	88	124
	R^2	-		0.6678	0.7459	0.7020	0.7151
PSO model	k_2	g/mg · min	0.0057	0.0016	0.0004	0.0003
	q_e	mg g^{-1}	52	99	182	244
	R^2	-		0.9983	0.9966	0.9844	0.9802
	H	mg g^{-1} · min	15.41	15.67	14.20	16.80
ID model	k_{id}	mg gmin^0.5	1.90	5.10	13.13	18.46
	C_{id}	mg g^{-1}	34.49	49.20	47.10	53.65
	R^2	-		0.7122	0.7734	0.7305	0.7476

TABLE 5 Results of interpretation of kinetic models.

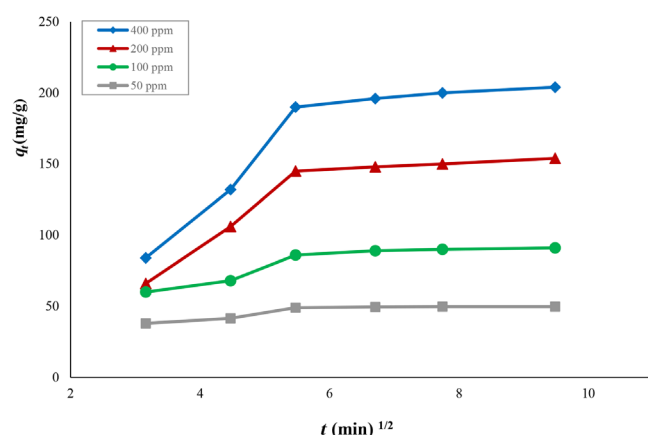Abbreviations: ID, intraparticle diffusion; PFO, pseudo first order; PSO, pseudo second order.

FIGURE 13 Intraparticle diffusion plots for different Pb^{2+}concentrations.

3.5 | Simulink simulation for the kinetics of adsorption process

The present research was done at the lab scale using a complete mixed reactor (CMR) which can be modelled in a Simulink platform (MATLAB software). In the kinetic section, PSO was selected as the best model. The schematic plan of Simulink modelling is presented in Figure S6. Based on our kinetic study, simulation practices were performed for 50, 100, 200, and 400 mg L^{-1} Pb^{2+} at the optimum conditions. The trends of Pb^{2+} elimination in reacting with NiCo-LDHs-rGO are illustrated in Figure 14. All the mentioned trends have been computed by using the numerical analysis of kinetic differential equations in the Simulink platform. According to Figure 14, it is found that the concentration of Pb^{2+} decreases in a 30 min run (adsorption process). Figure 15 presents q_t versus t, based on the numerical and experimental values.

The main purpose of this scheme is to evaluate the simulated kinetic model with the kinetic experimental outputs.

Considering Figure 15, it is clear that the simulated model is appropriately precise for the prediction of q_t in time series. It is worth noting that at those concentrations below 100 mg L^{-1}, the simulation and laboratory curves converge, while at higher concentrations, the convergence becomes lower and then the curves diverge. The reason for low convergence at high concentration can be a result of the desorption process, which occurs during the adsorption process when the surface is saturated.

3.6 | Selectivity

The adsorption selectivity for Pb^{2+} was checked in a binary and mixed solution of Pb^{2+} with co-existing ions such as Zn^{2+}, Cu^{2+}, and Cd^{2+}. As shown in Figure S7A (for binary analysis) the uptake of Pb^{2+} using NiCo-LDHs-rGO was higher than those of the other metals, so that the selectivity was found to be Pb^{2+} > Cu^{2+} > Zn^{2+} > Cd^{2+}. This difference could be attributed to several factors including ionic radius, hydration, and electronegativity. The selectivity of NiCo-LDHs-rGO for Pb^{2+} in a mixed solution is presented in Figure S7B. Based on the results, the adsorption capacity of NiCo-LDHs-rGO for Pb^{2+} was higher compared to the other ions. Moreover, the proposed NiCo-LDHs-rGO composite was applied for the removal of Pb^{2+} from the synthetic and natural wastewater samples (supplied from an industrial factory in Mashhad, Iran; Table S3). According to the results, more than 90.0% of the Pb^{2+} contamination was removed by the NiCo-LDHs-rGO composite, indicating its high selectivity for the Pb^{2+} ion.

FIGURE 14 Outputs of Simulink kinetic simulation in different Pb^{2+} concentrations such as (A) 50 mg L^{-1}, (B) 100 mg L^{-1}, (C) 200 mg L^{-1}, and (D) 400 mg L^{-1}.
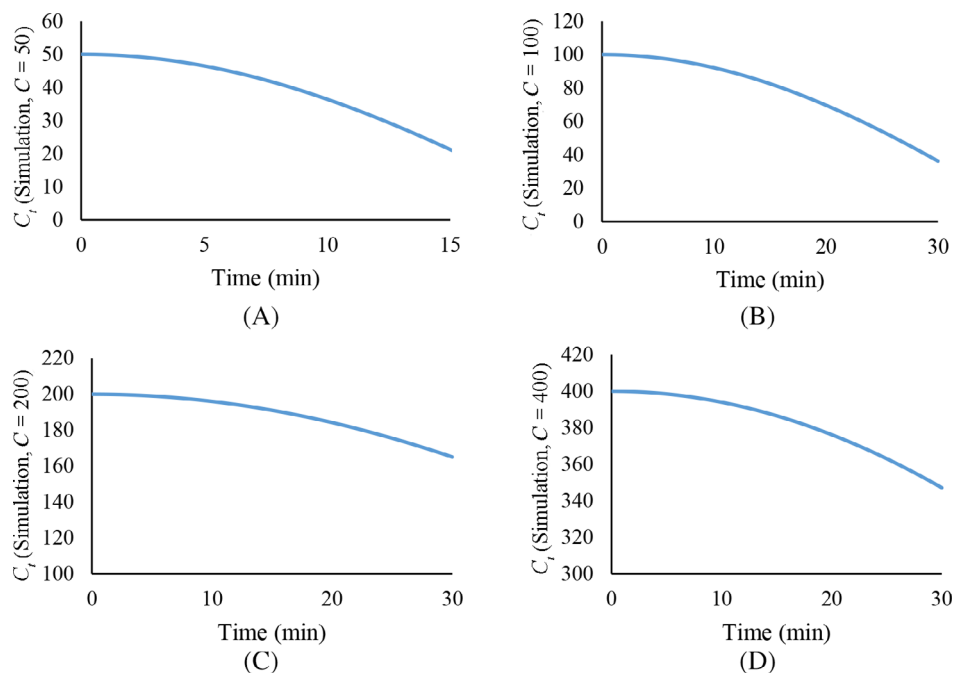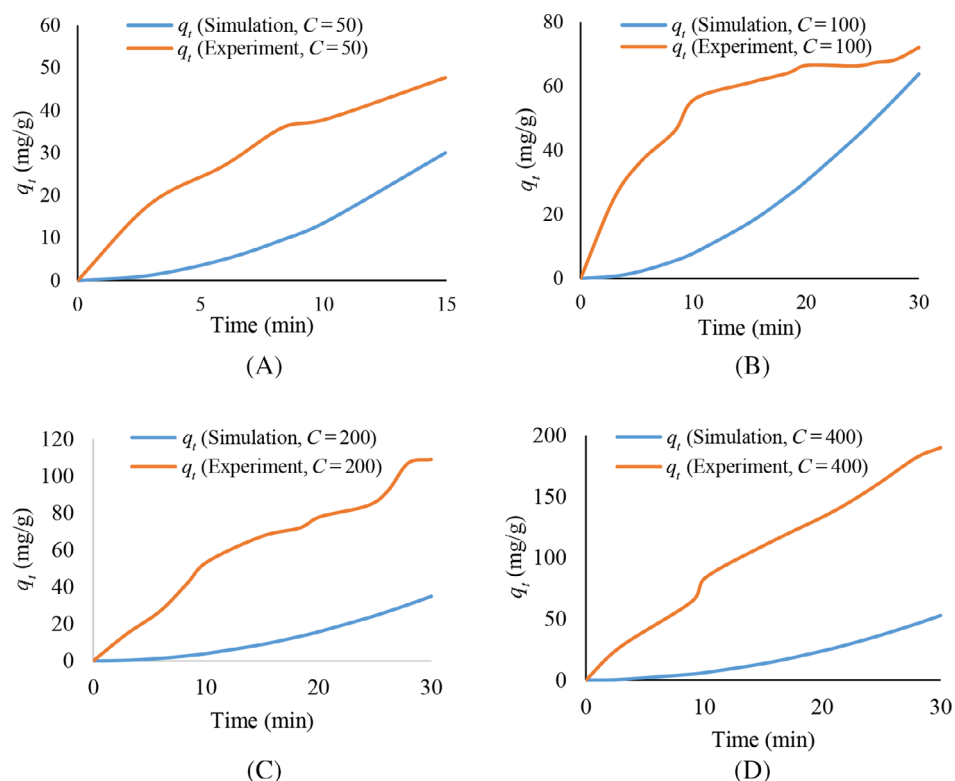

FIGURE 15 Experimental/ simulation kinetic evaluations of adsorption capacity outputs based on the Simulink simulation for (A) 50 mg L^{-1}, (B) 100 mg L^{-1}, (C) 200 mg L^{-1}, and (D) 400 mg L^{-1}.

3.7 | Reusability of adsorbent

The reusability of NiCo-LDHs-rGO was investigated by seven replicated adsorption/desorption cycles using HCl (0.01 mol L^{-1}) as the desorbent solution. The results in Figure S8 confirm that the RP of Pb^{2+} decreases by 12.0% after the fourth cycle; however, it remains at approximately 87.0% (for 100 mg L^{-1} of Pb^{2+}). Finally, in the seventh cycle, the RP dropped to 70.0%, indicating that this composite can be used at least for seven times with only 20.0% reduction in RP.

3.8 | Comparison with other adsorbents

Table S4[52–58] presents a comparison between our synthesized NiCo-LDHs-rGO composite and other adsorbents used for the decontamination of water samples.

Considering the advantages of NiCo-LDHs-rGO—such as high adsorption capacity (200 mg g^{-1}), rapidity (30 min), and green and convenient synthetic approach (one-step synthesis)—it is a great and efficient adsorbent for the removal of Pb^{2+}.

4 | CONCLUSION

In this study, a NiCo-LDHs-rGO composite was synthesized using a hydrothermal method and fully characterized by FT-IR, FESEM, EDX, mapping elemental analysis, XRD, and BET analysis. Also, NiCo-LDHs-rGO was successfully employed in the removal of Pb^{2+} from water samples. The advantages of this method include a one-step synthesis of the adsorbent, short removal time, and remarkably high adsorption capacity. The experimental results indicated that this composite has the maximum efficiency at pH 5.0 (99.7% for 100 mg L^{-1} of Pb^{2+}). Also, the presence of co-existence ions did not significantly affect the removal process at optimum experimental conditions. The experimental adsorption isotherm data were well fitted with the Freundlich isotherm model ($q_{\max} = 200.0$ mg g^{-1}), while the PSO kinetic model was the best equation for the interpretation of kinetic results. Moreover, the performance of the composite adsorbent did not change considerably after four regeneration cycles (nearly 87.0% RP), suggesting that the NiCo-LDHs-rGO composite is a promising and economic material for the removal of Pb^{2+}. This composite is an inexpensive and suitable material for the decontamination of wastewater.

AUTHOR CONTRIBUTIONS
Ata Makarem: Writing – original draft; formal analysis; conceptualization; validation; investigation; writing – review and editing. **Alireza Aldaghi:** Investigation; writing – original draft; methodology; data curation. **Mohammad Gheibi:** Conceptualization; investigation; writing – original draft; validation; methodology; writing – review and editing; formal analysis; software; data curation. **Mohammad Eftekhari:** Conceptualization; investigation; writing – original draft; validation; methodology; writing – review and editing; project administration; formal analysis; data curation; supervision. **Kourosh Behzadian:** Investigation; methodology; writing – original draft; formal analysis; supervision; conceptualization; project administration; data curation; writing – review and editing.

CONFLICT OF INTEREST STATEMENT
The authors declare no competing financial interest.

DATA AVAILABILITY STATEMENT
The data that support the findings of this study are available from the corresponding author upon reasonable request.

REFERENCES
[1] G. Flora, D. Gupta, A. Tiwari, *Interdiscip. Toxicol.* **2012**, *5*, 47.

[2] G. J. May, A. Davidson, B. Monahov, *Journal of Energy Storage* **2018**, *15*, 145.

[3] A. Goyal, S. McKechnie, D. Pashov, W. Tumas, M. van Schilfgaarde, V. Stevanović, *Chem. Mater.* **2018**, *30*, 3920.

[4] Centers for Disease Control and Prevention, Lead: CDC's National Surveillance Data (1997–2015) (Centers for Disease Control and Prevention, 2016), https://www.cdc.gov/nceh/lead/data/national.htm (accessed: March 2023).

[5] M. Tuzen, A. Sarı, T. A. Saleh, *Chem. Eng. Res. Des.* **2020**, *163*, 76.

[6] A. Sarı, T. A. Saleh, M. Tuzen, *Surf. Interfaces* **2021**, *27*, 101504.

[7] T. A. Saleh, M. Tuzen, A. Sarı, *Chem. Eng. Res. Des.* **2022**, *184*, 215.

[8] T. A. Saleh, M. Tuzen, A. Sarı, N. Altunay, *Chem. Eng. Res. Des.* **2022**, *183*, 181.

[9] I. Khan Rind, A. Sarı, M. Tuzen, M. Farooque Lanjwani, I. Karaman, T. A. Saleh, *Surf. Interfaces* **2023**, *38*, 102765.

[10] I. Khan Rind, M. Tuzen, A. Sarı, M. Farooque Lanjwani, N. Memon, T. A. Saleh, *Chem. Eng. Res. Des.* **2023**, *191*, 523.

[11] A. Shahat, R. Awual, A. Khaleque, Z. Alam, M. Naushad, A. M. Sarwaruddin Chowdhury, *Chem. Eng. J.* **2015**, *273*, 286.

[12] R. Awual, *J. Environ. Chem. Eng.* **2019**, *7*, 103087.

[13] R. Awual, A. Islam, M. Hasan, M. M. Rahman, A. M. Asiri, A. Khaleque, C. Sheikh, *J. Cleaner Prod.* **2019**, *224*, 920.

[14] R. Awual, M. Hasan, A. Islam, M. M. Rahman, A. M. Asiri, A. Khaleque, C. Sheikh, *J. Cleaner Prod.* **2019**, *231*, 214.

[15] A. Makarem, M. Gheibi, R. Mirsafaei, M. Eftekhari, *J. Mol. Liq.* **2023**, *388*, 122743.

[16] N. Rezazadeh, S. Danesh, M. Eftekhari, *J. Dispersion Sci. Technol.* **2023**, *44*, 889.

[17] Q. Zhang, Q. Hou, G. Huang, Q. Fan, *Environ. Sci. Pollut. Res.* **2020**, *27*, 190.

[18] J. Y. Lim, N. M. Mubarak, E. C. Abdullah, S. Nizamuddin, M. Khalid, *J. Ind. Eng. Chem.* **2018**, *66*, 29.

[19] M. Majdoub, A. Amedlous, Z. Anfar, A. Jada, N. El Alem, *J. Colloid Interface Sci.* **2021**, *589*, 511.

[20] A. Shahzad, W. Miran, K. Rasool, M. Nawaz, J. Jang, S. R. Lim, D. S. Lee, *RSC Adv.* **2017**, *7*, 9764.

[21] M. Eftekhari, M. Gheibi, M. Akrami, F. Iranzad, *New J. Chem.* **2018**, *42*, 1159.

[22] D. Ghadirimoghaddam, M. Gheibi, M. Eftekhari, *Int. J. Environ. Anal. Chem.* **2023**, *103*, 469.

[23] J. Cao, Q. Mei, R. Wu, W. Wang, *Electrochim. Acta* **2019**, *321*, 134711.

[24] J. Jiang, A. Zhang, L. Li, L. Ai, *J. Power Sources* **2015**, *278*, 445.

[25] M. V. Bukhtiyarova, *J. Solid State Chem.* **2019**, *269*, 494.

[26] M. F. Warsi, I. Shakir, M. Shahid, M. Sarfraz, M. Nadeem, Z. A. Gilani, *Electrochim. Acta* **2014**, *135*, 513.

[27] Y. Chen, T. Liu, L. Zhang, J. Yu, *ACS Sustainable Chem. Eng.* **2019**, *7*, 11157.

[28] Z. Lv, Q. Zhong, Y. Bu, *Adv. Mater. Interfaces* **2018**, *5*, 1800438.

[29] R. Li, Z. Hu, X. Shao, P. Cheng, S. Li, W. Yu, W. Lin, D. Yuan, *Sci. Rep.* **2016**, *6*, 18737.

[30] K. Satheesh, R. Jayavel, *Mater. Lett.* **2013**, *113*, 5.

[31] K. D. Klika, R. Alsalim, M. Eftekhari, A. Makarem, *Dalton Trans.* **2022**, *51*, 12436.

[32] M. Eftekhari, M. Akrami, M. Gheibi, H. Azizi-Toupkanloo, A. M. Fathollahi-Fard, G. Tian, *Environ. Sci. Pollut. Res.* **2020**, *27*, 43999.

[33] T. Dong, X. Zhang, M. Li, P. Wang, P. Yang, *Inorg. Chem. Front.* **2018**, *5*, 3033.

[34] Y. Ouyang, T. Xing, Y. Chen, L. Zheng, J. Peng, C. Wu, B. Chang, Z. Luo, X. Wang, *Journal of Energy Storage* **2020**, *30*, 101454.

[35] L. Zhang, P. Cai, Z. Wei, T. Liu, J. Yu, A. A. Al-Ghamdi, S. Wageh, *J. Colloid Interface Sci.* **2021**, *588*, 637.

[36] Y. Zheng, B. Cheng, J. Fan, J. Yu, W. Ho, *J. Hazard. Mater.* **2021**, *403*, 123559.

[37] X. Wang, B. Cheng, L. Zhang, J. Yu, Y. Li, *J. Colloid Interface Sci.* **2022**, *612*, 598.

[38] S. Salman, C. Sheikh, M. Hasan, N. Hasan, K. T. Kubra, et al., *Appl. Surf. Sci.* **2023**, *662*, 157008.

[39] S. Salman, N. Hasan, M. Hasan, K. Tul Kubra, C. Sheikh, A. Islam Rehan, R. M. Waliullah, A. Islam Rasee, E. Awual, M. S. Hossain, A. K. D. Alsukaibi, H. M. Alshammari, R. Awual, *J. Mol. Struct.* **2023**, *1282*, 135259.

[40] M. Hasan, K. Tul Kubra, N. Hasan, E. Awual, S. Salman, C. Sheikh, A. Islam Rehan, A. Islam Rasee, R. M. Waliullah, S. Islam, S. Khandaker, A. Khandaker, M. S. Hossain, A. K. D. Alsukaibi, H. M. Alshammari, R. Awual, *J. Mol. Liq.* **2023**, *371*, 121125.

[41] T. Saadati, M. Eftekhari, N. Rezazadeh, M. K. Nazarabad, *Int. J. Environ. Sci. Technol.* **2023**, *20*, 1301.

[42] M. Soylak, M. Tuzen, *J. Hazard. Mater.* **2006**, *137*, 1496.

[43] M. Soylak, R. Sungur Cay, *J. Hazard. Mater.* **2007**, *146*, 142.

[44] S. K. Karna, R. Sahai, *International Journal of Engineering, Science and Mathematics* **2012**, *1*, 1.

[45] A. Mitra, *Wiley Interdisciplinary Reviews: Computational Statistics* **2011**, *3*, 472.

[46] P. Yan, F. Li, Z. Liu, L. Li, *The International Journal of Advanced Manufacturing Technology* **2022**, *119*, 8039.

[47] R. Sips, *J. Chem. Phys.* **1948**, *16*, 490.

[48] R. A. Koble, T. E. Corrigan, *Industrial & Engineering Chemistry* **1952**, *44*, 383.

[49] J. Toth, *Acta Chim. Hung.* **1971**, *69*, 311.

[50] A. R. Khan, R. Ataullah, A. Al-Haddad, *J. Colloid Interface Sci.* **1997**, *194*, 154.

[51] K. Vijayaraghavan, T. V. N. Padmesh, K. Palanivelu, M. Velan, *J. Hazard. Mater.* **2006**, *133*, 304.

[52] R. Sahraei, M. Ghaemy, *Carbohydr. Polym.* **2017**, *157*, 823.

[53] M. Eftekhari, M. Gheibi, H. Azizi-Toupkanloo, Z. Hossein-Abadi, M. Khraisheh, A. M. Fathollahi-Fard, G. Tian, *Journal of Industrial Information Integration* **2021**, *23*, 100219.

[54] Y. Li, R. Zhao, S. Chao, B. Sun, C. Wang, X. Li, *Chem. Eng. J.* **2018**, *344*, 277.

[55] P. Pal, A. Pal, *J. Mol. Liq.* **2017**, *248*, 713.

[56] F. Vasheghani Farahani, M. H. Amini, S. H. Ahmadi, S. A. Zakaria, *J. Mol. Liq.* **2021**, *338*, 116774.

[57] Y. Zhang, Y. Liu, X. Wang, Z. Sun, J. Ma, T. Wu, F. Xing, J. Gao, *Carbohydr. Polym.* **2014**, *101*, 392.

[58] M. Yuan, T. Xie, G. Yan, Q. Chen, L. Wang, *Powder Technol.* **2018**, *332*, 234.

SUPPORTING INFORMATION

Additional supporting information can be found online in the Supporting Information section at the end of this article.